1521-0103/361/2/246–258$25.00
THE JOURNAL OF PHARMACOLOGY AND EXPERIMENTAL THERAPEUTICS

https://doi.org/10.1124/jpet.117.240523
J Pharmacol Exp Ther 361:246–258, May 2017

Physiologically Based Pharmacokinetic Model of All-*trans*-Retinoic Acid with Application to Cancer Populations and Drug Interactions[S]

Jing Jing, Cara Nelson, Jisun Paik, Yoshiyuki Shirasaka, John K. Amory, and Nina Isoherranen

Department of Pharmaceutics (J.J., C.N., Y.S., N.I.), Department of Medicine (J.A.), and Department of Comparative Medicine (J.P.), University of Washington, Seattle, Washington

Received February 1, 2017; accepted March 6, 2017

ABSTRACT

All-*trans* retinoic acid (*at*RA) is a front-line treatment of acute promyelocytic leukemia (APL). Due to its activity in regulating the cell cycle, it has also been evaluated for the treatment of other cancers. However, the efficacy of *at*RA has been limited by *at*RA inducing its own metabolism during therapy, resulting in a decrease of *at*RA exposure during continuous dosing. Frequent relapse occurs in patients receiving *at*RA monotherapy. In an attempt to combat therapy resistance, inhibitors of *at*RA metabolism have been developed. Of these, ketoconazole and liarozole have shown some benefits, but their usage is limited by side effects and low potency toward the cytochrome P450 26A1 isoform (CYP26A1), the main *at*RA hydroxylase. We determined the pharmacokinetic basis of therapy resistance to *at*RA and tested whether the complex disposition kinetics of *at*RA could be predicted in healthy subjects and in cancer patients in the presence and absence of inhibitors of *at*RA metabolism using physiologically based pharmacokinetic (PBPK) modeling. A PBPK model of *at*RA disposition was developed and verified in healthy individuals and in cancer patients. The population-based PBPK model of *at*RA disposition incorporated saturable metabolic clearance of *at*RA, induction of CYP26A1 by *at*RA, and the absorption and distribution kinetics of *at*RA. It accurately predicted the changes in *at*RA exposure after continuous dosing and when coadministered with ketoconazole and liarozole. The developed model will be useful in interpretation of *at*RA disposition and efficacy, design of novel dosing strategies, and development of next-generation *at*RA metabolism inhibitors.

Introduction

All-*trans* retinoic acid (*at*RA) is an active metabolite of vitamin A (retinol), circulating at endogenous plasma concentration of about 2 nM in healthy humans (Jing et al., 2016). One of the main biologic activities of *at*RA is regulating the cell cycle by binding to the nuclear retinoic acid receptors (RARs). Via RAR activation, *at*RA controls the expression of target genes involved in differentiation, cell cycle arrest, and apoptosis in a concentration-dependent manner.

Because of its activity in inducing apoptosis, *at*RA has been pursued for the treatment of various cancers including non-small-cell lung cancer, head and neck cancer, astrocytoma, and Kaposi's sarcoma (Phuphanich et al., 1997; Saiag et al., 1998; Arrieta et al., 2010; Lim et al., 2012). In acute promyelocytic leukemia (APL), promyelocyte differentiation is blocked due to the formation of promyelocytic leukemia-RARα fusion protein caused by the chromosomal translocation between chromosomes 15 and 17. Therapeutic doses of *at*RA resulting in a peak plasma concentration of 1 μM (Adamson, 1996) can overcome the blockage and trigger RAR-mediated promyelocyte differentiation (Ablain and de The, 2011). As monotherapy, *at*RA induces clinical remissions in 70%–90% of APL patients, but relapses are observed if *at*RA is continued as a single agent, so combination therapies are required for long-term disease control (Coombs et al., 2015). The loss of *at*RA efficacy is believed to be largely due to the 42%–62% reduction of plasma concentrations of *at*RA upon chronic dosing caused by autoinduction of *at*RA clearance (Muindi et al., 1992a; Regazzi et al., 1997; Russo et al., 1998; Ozpolat et al., 2003). This induction is likely due to increased expression of the cytochrome P450 isoform 26A1 (CYP26A1), the main *at*RA hydroxylase in human liver (Tay et al., 2010; Topletz et al., 2015).

This work was supported in part by funding from the National Institutes of Health National Institute of General Medical Sciences [Grant R01 GM111772] and the *Eunice Kennedy Shriver* National Institute of Child Health and Human Development through cooperative agreement [Grant U54 HD42454] as part of the Cooperative Contraceptive Research Centers Program.
https://doi.org/10.1124/jpet.117.240523.
[S] This article has supplemental material available at jpet.aspetjournals.org.

ABBREVIATIONS: APL, acute promyelocytic leukemia; atRA, all-trans retinoic acid; AUC, area under plasma concentration–time curve; BID, twice a day; CI, confidence interval; CL_{po}, oral clearance; DDI, drug-drug interaction; E_{max}, maximum fold induction; $f_{u,inc}$, fraction of unbound drug in the in vitro incubation; ISEF, intersystem extrapolation factor; LC-MS/MS, liquid chromatography with tandem mass spectrometry; PBPK, physiologically based pharmacokinetics; PO, by mouth; RAR, retinoic acid receptor; TEER, transepithelial electrical resistance; V_{ss}, steady-state volume of distribution.

To overcome the autoinduction of *at*RA clearance and increase systemic *at*RA concentrations, inhibitors of *at*RA metabolism have been developed. The decline of *at*RA area under the plasma concentration–time curve (AUC) after continuous oral treatment was attenuated by ketoconazole, a pan-CYP inhibitor, in advanced lung cancer patients (Rigas et al., 1993). Liarozole, an inhibitor of *at*RA metabolism, was found to partially reverse the decline of *at*RA AUC after chronic administration to patients with solid tumors (Miller et al., 1994).

Despite these promising clinical results, the use of *at*RA metabolism inhibitors in cancer therapy has been limited due to the adverse effects and lack of satisfactory potency and selectivity for the primary *at*RA metabolizing enzymes (Njar et al., 2006; Nelson et al., 2013). To develop more potent and selective inhibitors and efficient dosing strategies, a better understanding of *at*RA disposition and kinetics of induction of *at*RA metabolizing enzymes is needed.

CYP26A1 is predicted to be responsible for more than 90% of hepatic *at*RA clearance, although CYP2C8, CYP3A4, and CYP3A5 also metabolize *at*RA (Thatcher et al., 2010). The induction of *at*RA metabolism upon multiple dosing is likely caused by increased CYP26A1 enzyme expression because *at*RA treatment significantly induces CYP26A1 mRNA and activity in HepG2 cells and human hepatocytes (Tay et al., 2010; Topletz et al., 2015). However, the quantitative findings of CYP26A1 activity, *at*RA concentration-dependent induction of *at*RA metabolism, and the magnitude of pharmacokinetic changes in different populations receiving *at*RA have not been integrated into a model of *at*RA disposition in humans that could be applied to the design of better inhibitors of *at*RA metabolism or improved dosing regimens in *at*RA therapy. We hypothesized that physiologically based pharmacokinetic (PBPK) modeling and simulation could be used as a mechanistic tool to comprehensively understand the dose- and time-dependent disposition of *at*RA in different populations in the presence and absence of inhibitors of *at*RA metabolism.

PBPK modeling, which integrates physiologic parameters such as blood flow, tissue sizes, and composition with drug-specific parameters, is widely applied to simulate drug disposition in plasma and tissues (Jones et al., 2015). Uniquely altered physiologic parameters in different populations and disease states can be integrated into PBPK models to investigate variable drug disposition in humans. PBPK modeling also provides the possibility to simulate population variability and time-varying phenomena, including induction and saturation of clearance pathways. Therefore, PBPK modeling is exceptionally well suited to study *at*RA disposition. Surprisingly, existing *at*RA PBPK models (Clewell et al., 1997; Louisse et al., 2015) have not incorporated the induction of *at*RA metabolism or multiple dosing scenarios, or been applied to any disease population. We developed a full *at*RA PBPK model incorporating human physiology and *at*RA specific pharmacokinetic parameters to predict *at*RA disposition in humans after single and multiple doses of *at*RA in the absence and presence of *at*RA metabolism inhibitors in both healthy subjects and in cancer patients.

Materials and Methods

Chemicals and Reagents. Ketoconazole, *at*RA, and acitretin were purchased from Sigma-Aldrich (St. Louis, MO). *at*RA-d_5 was purchased from Santa Cruz Biotechnology (Santa Cruz, CA). We purchased 4OH-*at*RA and 4oxo-*at*RA-d_3 from Toronto Research Chemicals (North York, ON, Canada). Liarozole was purchased from Tocris Bioscience (Bristol, United Kingdom). CYP3A4 and CYP2C8 supersomes coexpressed with reductase and b_5 were purchased from BD Gentest (BD Biosciences, San Jose, CA). NADPH and high-pressure liquid chromatography-grade ethyl acetate were purchased from EMD Millipore (Billerica, MA). CYP26A1 was expressed in Sf9 insect cells and microsomes containing CYP26A1 were prepared as described elsewhere (Lutz et al., 2009). CYP26A1 content was measured by CO spectrum. Rat cytochrome P450 oxidoreductase was expressed in *Escherichia coli* and purified as described elsewhere (Lutz et al., 2009). Liquid chromatography with tandem mass spectrometry (LC-MS/MS) mobile phase solvents (water, acetonitrile, and methanol) were Optima grade and purchased from Fisher Scientific (Pittsburgh, PA).

***at*RA and 4OH-*at*RA Quantification.** All analyses were done using AB Sciex 5500 qTrap Q-LIT mass spectrometer (Foster City, CA) equipped with an Agilent 1290 UHPLC (Santa Clara, CA) using validated analytic methods described elsewhere (Arnold et al., 2012, 2015; Jing et al., 2016). Sample preparation methods are described here for each type of sample. For the analysis of *at*RA-d_5 and *at*RA concentrations in mouse serum and tissue samples, human blood and plasma samples, Caco-2 cell permeability assay, and *at*RA depletion in CYP26A1 inhibition assay, *at*RA-d_5 and *at*RA were separated using an Ascentis Express RP-Amide column (2.7 μm, 15 cm $\times$ 2.1 mm; Sigma-Aldrich). A gradient elution with aqueous (A) and acetonitrile (B) with 0.1% formic acid and 40% methanol in both A and B was used. The gradient was from initial 60% A for 2 minutes to 45% A over 8 minutes, then to 10% A over 7 minutes, and finally held at 5% A for 3 minutes before re-equilibration. Mobile phase flow was 0.5 ml/min. Analytes were detected using positive ion atmospheric-pressure chemical ionization mode. MS/MS transitions for *at*RA, *at*RA-d_5 (internal standard for *at*RA assay), and acitretin (internal standard for *at*RA-d_5 assay) were *m/z* 301 $>$ 205, *m/z* 306.1 $>$ 127.2, and *m/z* 327.0 $>$ 77, respectively. The declustering potential, collision energy, and collision exit potential were 80, 17, and 10 for *at*RA, 46, 23, and 8 for *at*RA-d_5 and 46, 77, and 14 for acitretin. A minimum of six quality control samples prepared in the relevant matrix were included in each LC-MS/MS run.

The formation of *at*RA metabolite 4OH-*at*RA in CYP2C8 and CYP3A4 inhibition assays was measured as described elsewhere (Topletz et al., 2015). The 4OH-*at*RA was separated using an Agilent Zorbax Extend C18 column (3.5 μm, 2.1 $\times$ 100 mm; Agilent Technologies) with a gradient elution at a flow rate of 0.3 ml/min. The gradient was from initial 95% of aqueous with 0.1% formic acid (A) and 5% of acetonitrile (B) to 5% A over 5.5 minutes, then held for 1 minute before re-equilibration to initial conditions. Analytes were detected using positive ion electrospray ionization mode. The declustering potential, collision energy, and collision exit potential were set to 80, 30, and 13 for 4OH-*at*RA and 80, 35, and 2 for 4oxo-*at*RA-d_3 (internal standard). The tandem mass spectrometry transitions for 4OH-*at*RA and 4oxo-*at*RA-d_3 were *m/z* 299.2 $>$ 197.2 and *m/z* 300.0 $>$ 226.0, respectively.

***at*RA Blood to Plasma Ratio.** The blood to plasma ratio of *at*RA was measured in fresh human blood collected into EDTA-containing tubes to avoid clotting. We spiked *at*RA-d_5 into 600-μl aliquots of blood in triplicate with 25 nM final concentration. Samples were mixed and incubated at 37°C for 2 hours. After incubation, 120 μl of whole blood was removed, and protein was precipitated with 120 μl acetonitrile. The remaining sample was centrifuged at 16,100*g* for 5 minutes at room temperature to pellet red blood cells and isolate plasma. Then 120 μl of acetonitrile was added to 120 μl of plasma to precipitate plasma proteins. We added 2 μl of 10 μM acitretin to all samples as the internal standard. Samples were centrifuged at 3000*g* for 15 minutes at 4°C, 100 μl of supernatant was transferred to glass vials, and samples were analyzed using LC-MS/MS as described earlier.

***at*RA Permeability in Caco-2 Cells.** Caco-2 cells were cultured at 37°C in a humidified atmosphere of 5% CO_2 using Dulbecco's modified Eagle's medium supplemented with 10% fetal bovine serum, 1% L-glutamine, 1% nonessential amino acids, and 5% antibiotic-antimycotic solution. Cells were routinely subcultured at 90% confluency with trypsin-EDTA. Caco-2 cells were plated onto cell culture inserts (3.0 μm pores, 0.9 cm^2 growth area) at a density of 6.4×10^4 cells/insert. The culture medium (0.8 ml in the insert and 2.0 ml in the well) was replaced with fresh medium at day 5 after initiation of cell culture and every 48 hours thereafter.

After 21 days in culture, the Caco-2 monolayer was used for the permeability experiments. Cell monolayers were preincubated in transport medium (Hank's balanced salt solution; 0.952 mM $CaCl_2$, 5.36 mM KCl, 0.441 mM KH_2PO_4, 0.812 mM $MgSO_4$, 136.7 mM NaCl, 0.385 mM Na_2HPO_4, 25 mM D-glucose, and 10 mM HEPES, pH 7.4) for 30 minutes at 37°C. After preincubation, the transepithelial electrical resistance (TEER) was measured routinely with a Millicell-ERS system (Millipore, Bedford, MA) to ensure cell monolayer integrity. The cell monolayers that exhibited TEER values higher than 500 $\Omega \cdot cm^2$ were used for experiments.

Permeability measurement was initiated by adding test compounds (10 μM) to the donor side and transport medium to the receiver side. Transfer of test compounds was observed in two directions, apical to basolateral and basolateral to apical. Samples were obtained from the donor side at 5 minutes for measurement of initial concentration and from the receiver side at 30, 60, 90, 120, and 180 minutes. Permeability experiments were performed under no pH gradient condition (apical pH = basal pH = 7.4) at 37°C. After all experiments, TEER was measured to ensure cell monolayer integrity, and data were generated in cell monolayers in which viability had not been adversely affected by the experimental conditions were accepted.

The apparent permeability (P_{app}, cm/s) of test compounds across cell monolayers was calculated using eq. 1:

$$P_{app} = \frac{dQ}{dt} \frac{1}{A \cdot C_D} \quad (1)$$

where Q is the amount of compound transported over time t (therefore, dQ/dt is the amount of compound transported within a given time period [μmol/s]). C_D is the initial concentration of compound in the donor compartment (μM), and A is the membrane surface area (cm^2). The concentration of *at*RA was analyzed by LC-MS/MS as described earlier. For all transport assays, atenolol and metoprolol were used as controls, and the LC-MS/MS methods for these compounds are described in supplemental data.

Tissue Distribution of *at*RA-d_5 in C57BL/6J Mice. Disposition of *at*RA was characterized and tissue to plasma partition coefficients (K_p) were determined in C57BL/6J mice. Animal experiments were approved by the University of Washington's Institutional Animal Care and Use Committee. For the study, 12 male C57BL/6J mice were dosed with 1 mg/kg *at*RA-d_5 i.p., and blood, liver, kidney, and pancreas were collected at 0.5, 1, 2, and 4 hours after dosing under yellow light. Three mice were sacrificed at each time point. In addition, three mice were dosed with vehicle and sacrificed immediately after vehicle administration. At each time point serum was separated from blood by centrifugation, samples were protected from light, and each tissue sample was snap frozen in liquid nitrogen and stored in −80°C until analysis.

Tissue homogenization and *at*RA-d_5 extraction were performed as described elsewhere (Arnold et al., 2015). In brief, 100 mg of tissue per sample was homogenized in a 1:1 volume of 0.9% NaCl, and *at*RA-d_5 was extracted with 10 ml of hexanes after addition of 10 μM acitretin as an internal standard. After evaporation of the organic layer under nitrogen, the sample was reconstituted with 65 μl of 60:40 acetonitrile/H_2O, and the concentration of *at*RA-d_5 was measured using LC-MS/MS as described earlier.

For the pharmacokinetic analysis, the area under the tissue or serum concentration versus time curve from time 0 to infinity ($AUC_{0-\infty}$) was calculated by standard noncompartmental analysis with Phoenix (St. Louis, MO) using a linear trapezoidal method. K_p was calculated using eq. 2 with conversion of serum AUC from h · pmol/ml to h · pmol/g, assuming 1 ml of serum = 1 g.

$$K_p = \frac{AUC_{0-\infty\,tissue}\ h \cdot pmol/g}{AUC_{0-\infty\,serum}\ h \cdot pmol/g} \quad (2)$$

Development of *at*RA PBPK Model in Healthy Humans. A PBPK model of *at*RA was constructed using Simcyp population-based ADME simulator v.14 (Certara, Sheffield, UK) using a full PBPK model (Fig. 1A), and the model was developed and verified according to the workflow shown in Fig. 1B. The absorption kinetics of *at*RA was simulated with first-order absorption model using the Caco-2 cell permeability data and the absorption kinetics of *at*RA observed in healthy volunteers. In brief, the fraction absorbed (F_a) and a nominal flow in gut model (Q_{gut}) were predicted using *at*RA Caco-2 cell permeability data within Simcyp. The k_a and lag time were estimated using the observed concentration–time profiles from three studies in healthy volunteers administered with a single oral dose of *at*RA (Ozpolat et al., 2003; Thudi et al., 2011; Peng et al., 2014). The reported concentration–time profiles were digitized using Plot Digitizer software (http://plotdigitizer.sourceforge.net), and one compartment pharmacokinetic model with first-order absorption was fitted to the data using Phoenix WinNonlin 6.4 (Pharsight Corporation, Cary, NC).

For *at*RA distribution, a full PBPK model was used. Because intravenous *at*RA studies are not available in humans, steady-state volume of distribution (V_{ss}) in humans was first predicted using allometric scaling from studies in adult Wistar rats and *Macaca fascicularis* monkeys after administration of *at*RA intravenously (Sandberg et al., 1994; Saadeddin et al., 2004). The V_{ss} of *at*RA in adult humans was estimated using the allometric equation:

$$Y = a \times W^b \quad (3)$$

where Y is V_{ss} (l), W is body weight (kg), and a and b are the allometric coefficient and exponent, respectively. The K_p values were independently predicted in Simcyp using the method described by Rodgers and Rowland (2006). The K_p values for liver, kidney, and pancreas were then refined based on data from the mouse pharmacokinetic study described earlier. For the lung and brain, the K_p values were refined based on reported literature values (Wang et al., 1980). To achieve concordance between the allometric scaling V_{ss} and in silico predicted V_{ss}, a K_p value of 0.2 was assigned to all other tissues except those mentioned previously.

The hepatic clearance of *at*RA was predicted using previously reported enzyme kinetic data for CYP2C8, CYP3A4, CYP3A5, CYP3A7, and CYP26A1 (Thatcher et al., 2010). Intersystem extrapolation factor (ISEF) of CYP2C8, CYP3A4, CYP3A5, and CYP3A7 used Simcyp default values for BD supersomes as 0.43, 0.24, 0.24, and 0.24, respectively. For CYP26A1, the ISEF value of 0.14 was calculated based on the reported ratio between the predicted *at*RA clearance (171.0 ± 99.5 μl/min/mg) from recombinant insect cell microsome data and the observed clearance (23.2 ± 20.4 μl/min/mg) obtained in human liver microsomes (Thatcher et al., 2010).

As the standard Simcyp population file does not have CYP26A1, CYP26A1 was incorporated into the population profile as CYP2J2 in the liver and gastrointestinal tract. In the liver, the protein abundance of 1.6 pmol/mg protein (63% CV) was assigned for CYP26A1 enzyme abundance according to the literature (Thatcher et al., 2010). The CYP26A1 turnover half-life was estimated between 24 and 48 hours with the turnover rate constant (k_{deg}) of 0.029–0.014 $hour^{-1}$ based on the in vitro data (Topletz et al., 2015). A sensitivity analysis of k_{deg} in the range of 0.029–0.014 $hour^{-1}$ was conducted with less than 20% difference on the predicted *at*RA AUC. Based on this, a turnover rate constant for CYP26A1 was estimated at 0.014 $hour^{-1}$ and used in this model. Because both the CYP26A1 mRNA and protein levels were low in human intestine (Topletz et al., 2012), 0 was assigned to CYP26A1 enzyme abundance in the gastrointestinal tract.

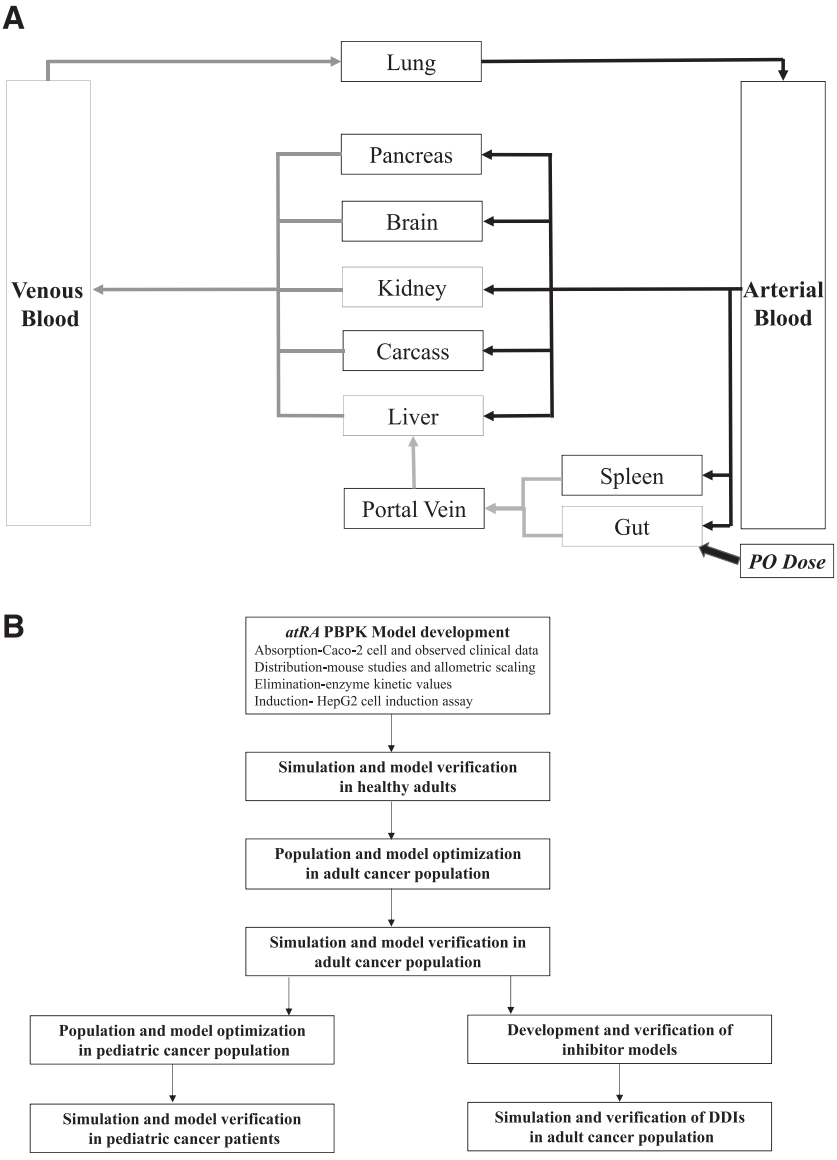

Fig. 1. Development of the *at*RA PBPK model. (A) The *at*RA PBPK model structure. (B) Workflow of model development and verification.

All-*trans* retinoic acid is known to induce the mRNA and protein expression of CYP26A1. The induction parameters determined previously in HepG2 cells were incorporated into the model. The maximum fold induction (E_{max}) of CYP26A1 by *at*RA was estimated between 22-fold and 44-fold based on the observed increase in formation of RA metabolites from *at*RA-d_5 in HepG2 cells after treatment with 1 μM *at*RA (Topletz et al., 2015), and an E_{max} of 33 was used for the model. A sensitivity analysis of E_{max} in the range of 22–44 was conducted with less than 15% difference in the predicted *at*RA AUC. Therefore, E_{max} of 33 was considered acceptable. An *at*RA concentration (0.09 μM) that supports half maximal induction (EC_{50}) was taken from the dose–response analysis of CYP26A1 induction by *at*RA after 24 hours of treatment in HepG2 cells (Tay et al., 2010). The fraction of unbound drug in the in vitro incubation ($f_{u,inc}$) of 0.4 was used in the model based on the literature (Topletz et al., 2015).

Simulation of *at*RA Disposition in Healthy Humans. To compare the simulated *at*RA disposition with the reported studies in healthy humans, PubMed searches were conducted using the search terms "retinoic acid pharmacokinetics" and "retinoic acid" in the title or abstract of the article. Three studies were found on *at*RA disposition in healthy volunteers (Ozpolat et al., 2003; Thudi et al., 2011; Peng et al., 2014). The observed concentration–time profiles from these publications were digitized using Plot Digitizer software (http://plotdigitizer.sourceforge.net). *at*RA pharmacokinetics were simulated using the Simcyp healthy volunteer profile with the modifications described earlier.

For one study (Peng et al., 2014) that was reported in Chinese, the Simcyp Chinese healthy volunteer profile was used with the modifications of the population as described earlier. The population profile was also modified to match the clinical study population for the age range and proportion of females.

For each study, 10 trials were simulated with the number (n) of subjects per trial matching that reported for that clinical study using random seed. The mean and standard deviation of the trials are reported. The dosing regimen was set identical to observed clinical studies. In the healthy volunteer studies, *at*RA was dosed either in mg basis or in mg/m^2 basis. All the studies were simulated using the same dosing units as reported in the clinical studies, and the data are reported with the matching dosing regimen as was originally reported. The validity of the model for healthy volunteers was evaluated by comparing the observed and simulated data using unpaired t test and by calculating the fold difference between the observed and predicted data.

Development of *at*RA PBPK model in Cancer Patients. The model of *at*RA disposition in cancer population was built based on the healthy population model with modifications on absorption kinetics and population parameters. To optimize the *at*RA PBPK model in adult cancer patients, F_a was estimated using bioavailability (F) calculated from published clinical studies in adult healthy subjects and cancer patients using eq. 4:

$$\frac{F_1 \text{ Dose}_1}{\text{AUC}_1} = \frac{F_2 \text{ Dose}_2}{\text{AUC}_2} \tag{4}$$

in which F_1 is the bioavailability in healthy subjects. Dose_1 (reported in mg/m^2) and AUC_1 are from a published clinical study in healthy subjects (Ozpolat et al., 2003). Dose_2 (reported in mg/m^2) and AUC_2 are the mean values from published clinical studies in cancer patients with the same dosage (Muindi et al., 1992a,b, 1994; Rigas et al., 1993, 1996; Miller et al., 1994; Adamson et al., 1995; Lee et al., 1995; Russo et al., 1998). Clearance of *at*RA was assumed to be identical in patients because the observed elimination half-life and t_{max} of *at*RA in healthy subjects matched the half-life and t_{max} observed in cancer patients with same single oral dose, but the maximum plasma concentration (C_{max}) and AUC were both altered in cancer patients. Therefore, F_a of 0.14 was used in the cancer population model. Due to the limited information on *at*RA disposition in healthy children and children with cancers, the F_a of 0.14 calculated from adult population was also used for the pediatric cancer population model.

The adult cancer population file was built based on the healthy adult population file with modifications of demographic parameters including age, sex, height, body weight, and blood composition including albumin, alpha-1-acid glycoprotein, and hematocrit to match the population parameters described elsewhere (Cheeti et al., 2013). For the pediatric population, the demographic parameters were kept the same as healthy children. CYP26A1 expression was incorporated in the cancer populations identically to that described earlier for the healthy population.

To compare the simulated *at*RA disposition with the reported studies in adult and pediatric cancer patients, PubMed searches were conducted using the search terms "retinoic acid pharmacokinetics" and "retinoic acid" in the title or abstract of the article, and studies that were conducted in cancer patients with sufficient pharmacokinetic data for evaluation were selected. Design of simulation trials was the same as described above for healthy subjects. In all of the reported *at*RA studies in patients the dose was reported as mg/m^2 basis, so the *at*RA dose in all the simulations was also set in mg/m^2 units. All the data are also reported for mg/m^2 dosing.

Model Verification. AUC was the primary variable used for model verification. For all populations for which only a single study existed at a given dosage level of *at*RA, an unpaired t test was used to compare whether the observed and predicted AUCs were significantly different from one another. For studies that were conducted at the same dosage level of *at*RA, acceptance criteria with the consideration of sample size and variance of the parameter of interest in reported studies were used. A prediction was considered acceptable if the predicted AUC was within the calculated upper and lower verification range of the observed AUC. The acceptance range of the mean simulated AUC was calculated as described elsewhere (Abduljalil et al., 2014) according to eqs. 5, 6, and 7,

$$\sigma = \sqrt{\ln\left[\left(\frac{\text{CV}\%}{100}\right)^2 + 1\right]} \tag{5}$$

$$A\bar{x} = \exp\left[\ln(\bar{x}) + 4.26\frac{\sigma}{\sqrt{N}}\right] \tag{6}$$

$$B\bar{x} = \exp\left[\ln(\bar{x}) - 4.26\frac{\sigma}{\sqrt{N}}\right] \tag{7}$$

where the calculated values A and B are the boundary values for fold difference between the predicted and observed AUC in a given study, $\bar{x}$ is the mean of the AUCs of *at*RA in all clinical studies giving the same dosing regimen, N is the sample size, and σ is the standard deviation of the AUC on the natural log scale. Due to the dose difference in reported clinical studies and dose- and time-dependent kinetics of *at*RA, the acceptance criteria (acceptable fold difference between observed and predicted) was calculated separately for each dose strength.

Determination of CYP Inhibition by Ketoconazole and Liarozole. To determine the inhibition potency of ketoconazole and liarozole toward *at*RA metabolism, the inhibition of *at*RA hydroxylation by ketoconazole and liarozole was evaluated using recombinant CYP3A4 and CYP2C8 as described elsewhere (Thatcher et al., 2011). Inhibition of CYP26A1 was tested by measuring the inhibition of *at*RA depletion. In brief, 5 pmol CYP3A4 and CYP2C8 supersomes were preincubated with ketoconazole or liarozole (≥7 concentrations of 0–100 μM) and 1 μM *at*RA for 5 minutes at 37°C in 1 ml 100 mM potassium phosphate buffer (KPi; pH 7.4). The reactions were initiated with addition of 1 mM NADPH and allowed to proceed for 10 minutes. Reactions were terminated by addition of 3 ml of ethyl acetate containing 100 pmol internal standard (4oxo-*at*RA-d_3). After centrifugation for 2 minutes to separate the organic and aqueous layers, the organic layer was collected then dried under nitrogen gas, and the sample was reconstituted with 100 μl of acetonitrile and analyzed by LC-MS/MS as described earlier.

To determine the inhibition of CYP26A1 by ketoconazole and liarozole, 0.1 pmol CYP26A1 was preincubated with 0.2 pmol reductase at room temperature for 5 minutes to allow the incorporation of reductase into the membrane. CYP26A1 with reductase was then preincubated with ketoconazole or liarozole (≥6 concentrations of 0–100 μM) and 2.5 nM *at*RA for 5 minutes at 37°C. Incubations (1 ml) were initiated by addition of 1 mM NADPH and quenched after 5 minutes with 5 ml of ethyl acetate containing. 15 pmol *at*RA-d_5 as an internal standard. The samples were centrifuged to separate the organic layer, dried under nitrogen, and reconstituted with 100 μl of acetonitrile before analysis with LC-MS/MS as described earlier. Depletion of *at*RA was determined in comparison with samples incubated in the absence of NADPH.

All experiments were performed in triplicate. The IC_{50} values were estimated by fitting eq. 8 to the data using nonlinear regression in GraphPad Prism (Graphpad Software, San Diego, CA).

$$\text{Activity remaining } \% = \frac{\textit{total activity}}{1 + 10^{([I] - \log(IC^{50}))}} \tag{8}$$

Total activity is the percentage of activity in the absence of inhibitor, $[I]$ is the concentration of ketoconazole or liarozole, and the IC_{50} is the concentration of inhibitor that causes 50% of the total measured inhibition.

Determination of Unbound Fraction of Ketoconazole and Liarozole in Supersomes and Plasma. The protein binding of the inhibitors was determined using ultracentrifugation as described elsewhere (Nakai et al., 2004; Shirasaka et al., 2013). To determine the unbound fraction in the in vitro incubations and in plasma, 100 μM of ketoconazole or liarozole was added to CYP3A4, CYP2C8, or CYP26A1 (5 pmol/ml) microsomes in KPi buffer or to plasma and the samples split into two aliquots. One aliquot was incubated at 37°C for 90 minutes; the other aliquot was centrifuged in a Sorvall Discovery M150 SE Ultracentrifuge at 100,000 rpm (435,630g) for 90 minutes at 37°C to precipitate protein. After centrifugation, 100 μl aliquots were transferred to a 96-well plate containing 100 μl acetonitrile.

A standard curve of each inhibitor was prepared in 50:50 KPi: acetonitrile (v: v) and analyzed in parallel. The samples were centrifuged using a Beckman Coulter Allegra 25R centrifuge at 3000g for 15 minutes at 4°C. After centrifugation, 100 μl from each well was transferred to a clean 96-well plate for LC-MS/MS analysis.

Samples were separated using a Shimadzu Prominence UFLC (Columbia, MD) equipped with a Thermo Hypersil Gold C18 column

(2.1 × 100 mm, 1.9 μm) using gradient elution with (A) H_2O (0.1% formic acid) and (B) acetonitrile at a flow rate of 0.5 ml/min. The gradient was from an initial 95% A to 10% A over 3 minutes, stayed at 10% A for 1.5 minutes, and then returned to 95% A for 2 minutes. Analytes were detected by an AB Sciex QTRAP 3200 mass spectrometer operated in electrospray positive mode with detection of *m/z* multiple reaction monitoring transition of 531.1/82.2 for ketoconazole and 309.14/241.1 for liarozole. The declustering potential, entrance potential, cell entrance potential, collision energy, and collision exit potential were set to 86, 5.5, 20, 73, and 6, respectively, for ketoconazole and 26, 4.5, 16, 17, and 4, respectively, for liarozole.

Development of Minimal PBPK Models for Ketoconazole and Liarozole. For the ketoconazole minimal PBPK model, ketoconazole-400 mg QD compound file in Simcyp was first verified with clinical observations. However, oral clearance (CL_{po}) (7.4 l/h) assigned in the compound file was generally lower than the reported average CL_{po} value (9.5 l/h) (Daneshmend et al., 1981, 1984; Baxter et al., 1986). Therefore, CL_{po} was optimized to 9.5 l/h with 30% CV. Because CL_{po} (14.4 l/h) in Simcyp ketoconazole-200 mg QD file was similar to the average CL_{po} (13.5 l/h) reported in the literature (Daneshmend et al., 1981, 1984; Huang et al., 1986), this file was used without modification on CL_{po}. For both models, the inhibition potency of ketoconazole toward CYP3A4, CYP2C8, and CYP26A1 as determined in the in vitro experiments was incorporated into the compound file.

The liarozole minimal PBPK model was built using information from the literature (Bryson and Wagstaff, 1996; De Buck et al., 2007) and in vitro experiments. The absorption of liarozole was described with first-order absorption model with Simcyp predicted absorption parameters. Elimination of liarozole was characterized using the CL_{po} reported in humans (Bryson and Wagstaff, 1996). Liarozole distribution was described using a minimal PBPK model with V_{ss} estimated from reported clinical data as 1.08 l/kg (Bryson and Wagstaff, 1996; Denis et al., 1998), and the elimination rate constant was calculated from eq. 9:

$$\frac{C_{ss,max}}{C_{ss,min}} = e^{k\tau} \tag{9}$$

in which $C_{ss,max}$ and $C_{ss,min}$ are the peak and trough concentrations at steady state, k is elimination rate constant, and τ is the dosing interval. The K_p value of liver was predicted using method 2 (Rodgers and Rowland, 2006) in Simcyp. In vitro measurements of $f_{u,mic}$ and K_i of liarozole for CYP2C8, CYP26A1, and CYP3A4 were incorporated into the interaction module. Because inhibition experiments were done at $S << K_m$, the IC_{50} can be assumed to be approximately equal to K_i, and IC_{50} values determined in the inhibition assay were used as K_i (Lutz and Isoherranen, 2012).

Results

***at*RA PBPK Model in Healthy Humans.** The *at*RA PBPK model in Simcyp was first developed in healthy humans based on obtained experimental and literature data. To develop the PBPK model, the blood to plasma ratio of *at*RA was measured. The blood to plasma ratio of *at*RA measured in human blood was 2.3, indicating significant partitioning into blood cells. To develop the PBPK model and establish tissue K_p values, we determined the *at*RA disposition in mice (Fig. 2). The elimination of *at*RA from serum after i.p. dosing was efficient with elimination half-life of 0.5 hours. Similar half-lives of 0.4 to 0.6 hours were observed in the liver, kidney, and pancreas, indicating fast metabolism of *at*RA in tissues and a rapid distribution equilibrium. The AUCs in the liver, kidney, and pancreas were higher than the AUC in serum (Table 1), indicating efficient partitioning of *at*RA into tissues. The measured K_p values of 3.79 and 2.06 in the liver and kidney, respectively, were similar to the K_p values calculated from the reported concentration–time data in mice after i.v. dosing with 10 mg/kg *at*RA (Wang et al., 1980). The K_p values predicted using Rodgers and Rowland method were 16.78, 10.14, 17.34, 2.28, and 26.90 for the liver, kidney, pancreas, lung, and brain, respectively, with a predicted V_{ss} of 28.10 l/kg. These values greatly exceeded the K_p values obtained from mouse studies. Similarly, the predicted V_{ss} significantly exceeded the V_{ss} of 0.46 l/kg predicted via allometric scaling. Therefore, the experimental K_p values were used to refine the distribution model (Table 2).

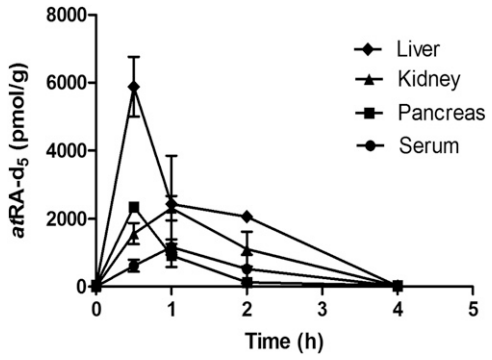

Fig. 2. Concentration–time profiles of *at*RA in C57BL/6J mouse (n = 12) serum, liver, kidney, and pancreas after administration 1 mg/kg *at*RA-d_5 i.p. Data are shown as mean ± S.D.

To predict the F_a and Q_{gut} in the first-order *at*RA absorption model, we measured the permeability of *at*RA in Caco-2 cells. In Caco-2 cells, a permeability of 3.58×10^{-6} cm/s was measured for *at*RA. The *at*RA permeability ratio (apical to basolateral/basolateral to apical) was 1.1, indicating that no active transporters were involved (Supplemental Fig. 1, Supplemental Table 1). The F_a of 0.48 and Q_{gut} of 3.5 l/h, were predicted based on Caco-2 cell permeability data indicating a low permeability for atRA in the gut. A k_a of 0.90 1/h with a 0.84-hour lag time for absorption was obtained from fitting the observed clinical data into one compartment model.

Due to the lack of dosage form, systemic *at*RA clearance has never been evaluated in humans. Clinical studies in humans after oral administration of *at*RA have reported that urinary excretion of unchanged *at*RA is negligible, and *at*RA is not found in human urine after β-glucuronidase incubation (Muindi et al., 1992b; Conley et al., 1997). Therefore, renal clearance and UDP-glucuronosyltransferase-mediated elimination were not incorporated into the model, and the clearance of *at*RA was all assigned to the hepatic P450 enzymes (Table 2). The complete model parameters are summarized in Table 2.

To verify the model, *at*RA disposition was first simulated in healthy subjects after administration of a single oral dose of

TABLE 1
Pharmacokinetic parameters of *at*RA obtained in male C57BL/6J mice (n = 12) dosed with 1 mg/kg *at*RA-d_5 i.p.

	$AUC_{0-\infty}$	C_{max}	t_{max}	$t_{1/2}$	K_p
	*h*pmol/g*	*pmol/g*	*h*	*h*	
Serum	1717	1168	1.0	0.5	
Liver	6503	5884	0.5	0.4	3.79
Kidney	3531	2316	1.0	0.4	2.06
Pancreas	1949	2358	0.5	0.6	1.13

TABLE 2
Summary of parameter input values for *at*RA PBPK model

Parameters	Input Values	Reference/Comment
Molecular weight (g/mol)	300.4	PubChem
log$P_{o:w}$	6.3	Drug bank
Compound type	Monoprotic acid	
pK_a	5	Drug bank
Blood-to-plasma ratio (B/P)	2.3	Measured
$f_{u,p}$	0.05	Muindi et al., 1992b
Absorption	1st order absorption model	
F_a		
Healthy population	0.48	Predicted
Cancer population	0.14	Predicted
k_a (1/h)	0.9	Assigned
Lag time (h)	0.84	Assigned
$f_{u,Gut}$	1	Simcyp default value
Q_{Gut} (l/h)	3.5	Predicted
$P_{eff,}$ man (10^{-4}cm/s)	0.5	Predicted
Distribution	Full PBPK model	
V_{ss} (l/kg)	0.46	Predicted
K_p		
Liver	3.79	Measured
Kidney	2.06	Measured
Pancreas	1.13	Measured
Lung	1.53	Wang et al., 1980
Brain	3.39	Wang et al., 1980
Other tissue	0.2/each	Assigned
Elimination	Enzyme kinetics: recombinant	
CYP3A4		
V_{max} (pmol/min/pmol p450)	4.0	Thatcher et al., 2010
K_m (μM)	19.4	Thatcher et al., 2010
$f_{u,mic}$	0.37	Thatcher et al., 2010
CYP2C8		
V_{max} (pmol/min/pmol p450)	4.8	Thatcher et al., 2010
K_m (μM)	13.4	Thatcher et al., 2010
$f_{u,mic}$	0.54	Thatcher et al., 2010
CYP26A1		
V_{max} (pmol/min/pmol p450)	11.3	Thatcher et al., 2010
K_m (μM)	0.0094	Thatcher et al., 2010
$f_{u,mic}$	1	Thatcher et al., 2010
CYP3A5		
V_{max} (pmol/min/pmol p450)	4.9	Thatcher et al., 2010
K_m (μM)	11.1	Thatcher et al., 2010
$f_{u,mic}$	0.31	Thatcher et al., 2010
CYP3A7		
V_{max} (pmol/min/pmol p450)	2.3	Thatcher et al., 2010
K_m (μM)	11.3	Thatcher et al., 2010
$f_{u,mic}$	0.3	Thatcher et al., 2010
Interaction	CYP26A1-induction	
Ind_{max}	33 (8.4 CV %)	Tay et al., 2010; Topletz et al., 2015
$IndC_{50}$ (μM)	0.09 (20.4 CV %)	Tay et al., 2010
$f_{u,inc}$	0.4	Topletz et al., 2015

*at*RA. Three different studies with *at*RA dosed at 10 mg, 20 mg, and 22.5 mg/m^2 by mouth (PO) were simulated. The observed mean concentration–time curves were within the 5th and 95th percentile of the simulated, and the mean simulated AUCs were 1.5-fold, 1.2-fold, and 0.9-fold of the observed ones (Fig. 3). The predicted AUCs for two of the three studies (70%) met the predefined acceptance criteria (simulated AUC not significantly different from observed, $P = 0.4$ and 0.7) and predicted C_{max} and t_{max} were similar to observed values (Table 3). The developed PBPK model successfully simulated the dose dependent kinetics of *at*RA after a single-dose administration with the oral clearance decreasing from 140 ± 136 l/h after a 10-mg dose to 87 ± 72 l/h after a 20-mg dose and to 65 ± 63 l/h after a 22.5-mg/m^2 dose of *at*RA.

To test whether the induction parameters for CYP26A1 would accurately predict the autoinduction of *at*RA clearance, the disposition of *at*RA after 22.5-mg/m^2 oral doses twice a day (BID) for 15 days was simulated (Fig. 3C). The predicted AUCs after multiple doses were not significantly different from the observed AUCs ($P = 0.1$ and 0.2) (Table 3). The simulated mean AUCs on days 9 and 15 were 0.6-fold and 0.5-fold, respectively, of the observed ones. The predicted 64% and 65% decreases in *at*RA AUC after multiple dosing were in good agreement with the observed 42% and 37% reductions of *at*RA AUC on days 9 and 15, respectively. Hence the developed model successfully simulated the saturation kinetics and autoinduction of *at*RA clearance, and based on these results the model was considered verified.

***at*RA PBPK Model in Adult and Pediatric Cancer Patients.** The *at*RA disposition in cancer patients was first simulated using the PBPK model developed in healthy population. Using the *at*RA drug file developed in healthy subjects overpredicted the AUC and C_{max} by about 5-fold and 3-fold whereas the t_{max} and half-life were accurately predicted.

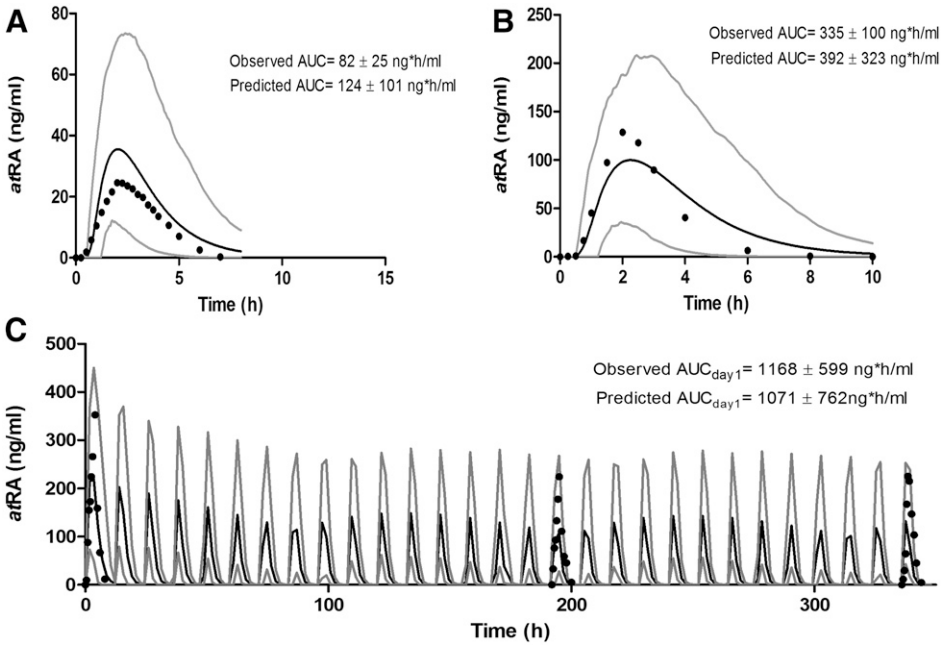

Fig. 3. Predicted and observed mean plasma concentration–time profiles of *at*RA in healthy volunteers. (A) Administration of 10-mg *at*RA PO (as described in Thudi et al., 2011). (B) Administration of 20 mg *at*RA PO (as described in Peng et al., 2014). (C) Administration of 22.5 mg/m^2 *at*RA PO BID (as described in Ozpolat et al., 2003). The solid line depicts the mean of the simulated data with 5th and 95th percentile shown with light gray line. Solid circles show the observed data in the study.

This suggested that F_a is decreased in cancer patients without changes in k_a, CL, or V. Therefore, F_a was optimized in the PBPK model from 0.48 to 0.14, and the population profile was modified according to published changes in cancer patients (Cheeti et al., 2013).

The *at*RA disposition was then simulated in 11 clinical studies conducted in cancer patients with *at*RA dosed at 40 mg/m^2 (two studies) and 45 mg/m^2 (nine studies). The predicted AUC for nine of the studies (82%) was within the predefined acceptance range, with mean simulated AUCs within 0.5-fold and 1.1-fold of the observed ones (Table 4). The observed mean AUC values in the two studies that were not accurately predicted were more than 2-fold different from the mean AUC of the other observed studies in cancer patients (Table 4). The observed AUC in the study conducted in large cell carcinoma and squamous cell carcinoma patients was <50% of the AUC values observed in the other studies with the same dosing regimen (Table 4). None of the other studies in cancer patients had a mean AUC that would have met the calculated acceptance range for the study in large cell carcinoma and squamous cell carcinoma patients. The observed AUC in one of the studies conducted in solid tumor patients had an observed AUC that was 2.7-fold to 3-fold higher than the mean *at*RA AUC observed in other studies in solid tumor patients, and none of the other studies in solid tumor patients had a mean AUC that would have met the calculated acceptance range for this study (Table 4). As such, neither the model nor the other clinical studies predicted the *at*RA AUCs in 2 of the 11 studies within the acceptance criteria. Unfortunately, the reported information on study populations was not sufficient to evaluate potential mechanisms of why these two studies showed discrepant disposition compared with other cancer studies.

The PBPK model in a cancer population also successfully simulated the dose-dependent kinetics of *at*RA with the simulated mean oral clearance decreasing from 335 l/h (two studies) to 276 l/h (nine studies) as the dose increased from 40 mg/m^2 to 45 mg/m^2 *at*RA. Similarly, the predicted AUCs of *at*RA were within the acceptance range on both day 1 and day 7 of dosing when compared with the observed data of multiple

TABLE 3

Observed and predicted pharmacokinetic parameters of *at*RA in healthy subjects (mean ± S.D.) after single dose (sd) and multiple doses (dosing regimen and duration specified)

Parameters	10 mg sd (n = 54)[a]	20 mg sd (n = 29)[b]	22.5 mg/m^2 BID		
			Day 1 (n = 11)[c]	Day 9 (n = 11)	Day 15 (n = 11)
AUC (ng·h/ml)					
Observed	82 ± 25	335 ± 100	1168 ± 599	676 ± 427	738 ± 742
Predicted	124 ± 101[d]	392 ± 323	1071 ± 762	385 ± 243	376 ± 240
C_{max} (ng/ml)					
Observed	33 ± 9	141 ± 32	508 ± 215	346 ± 235	376 ± 354
Predicted	38 ± 20	106 ± 54	264 ± 122	156 ± 75	154 ± 75
t_{max} (h)					
Observed	2.4 ± 0.9	2.1 ± 0.4	3.9 ± 2.9	3.1 ± 1.4	2.9 ± 1.5
Predicted	2.0 ± 0.4	2.3 ± 0.5	2.5 ± 0.5	2.0 ± 0.3	2.0 ± 0.3

[a]Data from Thudi et al., 2011.
[b]Data from Peng et al., 2014.
[c]Data from Ozpolat et al., 2003.
[d]Unpaired t test $P < 0.05$ between the observed and predicted AUC.

TABLE 4
Observed and predicted pharmacokinetic parameters of *at*RA in adult cancer patients (mean ± S.D.) after single and multiple doses

Diagnosis for Study Population	*n*	Dose	AUC			Reference
			Observed	Predicted	Acceptance range	
		mg/m²		*ng·h/ml*		
CMK day 1	18	40 BID	678 ± 498	438 ± 323	339–1356	Russo et al., 1998
CMK day 7	18	40 BID	259 ± 272	187 ± 115	130–518	Russo et al., 1998
Kaposi's sarcoma	8	40	725 ± 368	389 ± 322	363–1450	Adamson et al., 1995
LCC/SCC	21	45	162 ± 119	428 ± 264[a]	81–308	Rigas et al., 1996
Adenocarcinoma	22	45	571 ± 291	499 ± 316	286–1085	Rigas et al., 1996
Advanced NSCLC	31	45	467 ± 469	475 ± 329	234–887	Rigas et al., 1993
Solid tumors	13	45	1355 ± 1479	525 ± 403[a]	678–2575	Lee et al., 1995
Solid tumors	47	45	454 ± 419	510 ± 377	227–863	Muindi et al., 1994
Solid tumors	19	45	504 ± 549	505 ± 409	252–958	Miller et al., 1994
APL	10	45	499 ± 200	530 ± 388	250–948	Muindi et al., 1992a
APL	13	45	682 ± 500	545 ± 425	341–1296	Muindi et al., 1992b
APL	20	45	603 ± 442	561 ± 406	302–1146	Muindi et al., 1994

CMK, chronic myeloid leukemia; LCC, large cell carcinoma; SCC, squamous cell carcinoma; NSCLC, non-small cell lung cancer.
[a]Outside of verification range.

dosing study in chronic myeloid leukemia patients dosed with 40 mg/m^2 *at*RA BID (Table 4). The model predicted a 57% decrease in *at*RA AUC over the 7-day dosing which is in good agreement with the observed 62% reduction in *at*RA AUC on day 7.

Because *at*RA is frequently used in pediatric populations, the PBPK model was applied to a pediatric cancer population to simulate *at*RA disposition in pediatric patients. The *at*RA disposition after a single oral dose was simulated for three different studies with 30 and 40 mg/m^2 doses of *at*RA to pediatric cancer patients. The simulated mean AUC was 1.0-fold, 0.4-fold, and 0.5-fold of the observed values. The predicted AUC for two of the studies was within the predefined acceptance range (Table 5). For the third study with a higher dosing regimen, the predicted AUC was not significantly different from the observed ($P = 0.1$) and was within 2-fold of the observed. Similar to what was observed in adult clinical studies, the large variability in *at*RA kinetics was also observed in pediatric patients. The simulation of *at*RA disposition in adult and pediatric populations successfully captured this large variability (Tables 4 and 5).

PBPK Modeling of Effects of Ketoconazole and Liarozole on *at*RA Disposition. To predict the drug-drug interactions (DDIs) between *at*RA and ketoconazole and liarozole, the inhibition of *at*RA metabolism by ketoconazole and liarozole was first characterized in vitro (Fig. 4), and the results were incorporated into ketoconazole and liarozole models (Supplemental Tables 3 and 4).

Ketoconazole had the highest inhibition potency toward CYP3A4 (IC_{50} 0.015 μM; 95% confidence interval [CI], 0.010–0.023 μM), followed by CYP26A1 (IC_{50} 0.47 μM; 95% CI, 0.25–0.91 μM) and CYP2C8 (IC_{50}: 6.7 μM; 95% CI, 1.4–31 μM) (Fig. 4A). In contrast, liarozole had similar affinity to all three CYP isoforms with an IC_{50} of 3.3 μM (95% CI, 2.1–5.0 μM) for CYP26A1; 1.2 μM (95% CI, 0.92–1.6 μM) for CYP3A4; and 1.3 μM (95% CI, 0.77–2.3 μM) for CYP2C8 (Fig. 4B).

The ketoconazole PBPK models for different ketoconazole dosages were verified with clinical ketoconazole pharmacokinetic studies (Supplemental Fig. 2 and Supplemental Table 2), and the ketoconazole 200 mg PO dosing model and 400 mg PO dosing model were considered acceptable for DDI simulation. A liarozole PBPK model was also developed based on existing in vivo data (Supplemental Table 4), and liarozole disposition was simulated and compared with reported clinical studies (Supplemental Table 5). Due to the lack of information on the variability in liarozole disposition in the reported study, the liarozole model could not be verified using the acceptance criteria described. However, the predicted pharmacokinetic parameters were within the 2-fold range of the observed values and thus were considered to be similar to the reported parameters and acceptable for DDI simulation.

After model verification, a multiphase DDI study between ketoconazole and *at*RA was simulated. In the clinical study, cancer patients were treated with 45 mg/m^2 *at*RA on days 1, 2, 28, and 29 of treatment and with 45 mg/m^2 *at*RA BID for the remaining days 3 to 27. A single dose of 200 mg or 400 mg

TABLE 5
Observed and predicted pharmacokinetic parameters of *at*RA in pediatric cancer patients (mean ± S.D.) after single dose

n	Dose	AUC			Reference
		Observed	Predicted	Acceptance Range	
	mg/m²		*ng·h/ml*		
8	30	340 ± 141	340 ± 297	102–1020	Smith et al. (1992)
5	30	972 ± 990	364 ± 234	292–2916	Takitani et al. (1995)
8	40	1007 ± 631	535 ± 532[a]	N/A	Smith et al. (1992)

[a]Unpaired *t* test $P = 0.1$ between the observed and predicted AUC in the indicated study. Not significantly different from observed AUC.

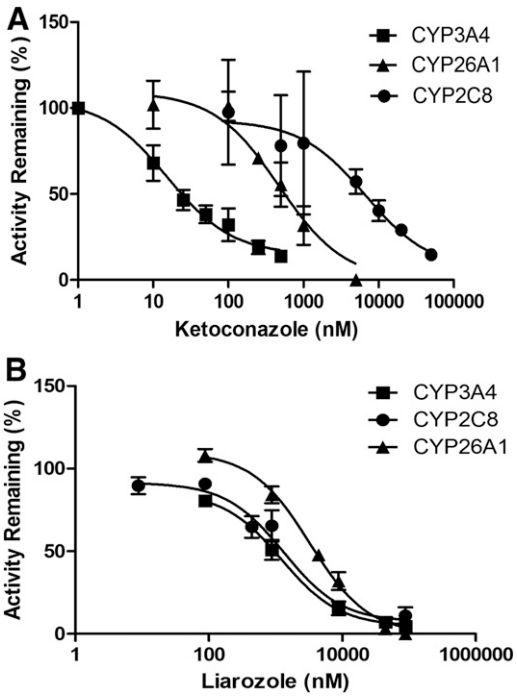

Fig. 4. In vitro IC_{50} curves for CYP26A1, CYP3A4, and CYP2C8 with *at*RA as substrate and ketoconazole and liarozole as inhibitors. Data are shown as mean ± S.D. (A) Ketoconazole CYP3A4 IC_{50}: 0.015μM; CYP26A1 IC_{50}: 0.47 μM; CYP2C8 IC_{50}: 6.65 μM. (B) Liarozole CYP3A4 IC_{50}: 1.22 μM; CYP26A1 IC_{50}: 3.26 μM; CYP2C8 IC_{50}:1.33μM.

ketoconazole was given on days 2 and 29, one hour before *at*RA (Rigas et al., 1993). The study was simulated using the verified ketoconazole PBPK model in the cancer population, and the simulation successfully predicted the DDI between *at*RA and ketoconazole in adult cancer patients (Table 6 and Fig. 5). The predicted AUC of *at*RA on each kinetic day in the presence and absence of ketoconazole met the acceptance criteria and was also within 2-fold of the observed (Table 6). The observed AUC on the first day was not available for the individual ketoconazole dosing groups and hence a single control group for *at*RA disposition was simulated.

The predicted decrease in *at*RA AUC between day 1 and day 28 of dosing was about 61% and in excellent agreement with the observed 61% decrease in *at*RA AUC. The inhibition of *at*RA clearance by ketoconazole was also well predicted. The simulation predicted a 1.4-fold increase in *at*RA AUC after ketoconazole administration on day 2, a fold increase similar to the observed average 1.1-fold increase in *at*RA AUC. The simulation also predicted a 2.0-fold and 2.7-fold increase in *at*RA AUC after 200 mg and 400 mg ketoconazole administration on day 29, a fold increase in excellent agreement with the observed 1.5-fold and 2.2-fold increases in *at*RA AUC between days 28 and 29. In context of predicting the efficacy of ketoconazole in combating therapy resistance, the model accurately predicted that 400-mg ketoconazole would restore the *at*RA exposure on day 29 to the levels observed on day 1.

Similar to the DDI study between ketoconazole and *at*RA, a DDI study between liarozole and *at*RA was simulated according to a reported study (Miller et al., 1994). In the reported study, cancer patients were treated with 45 mg/m^2 *at*RA on days 1, 2, 28, and 29 and with 45 mg/m^2 BID for the remaining days 3 to 27. A single dose of 75 mg, 150 mg, or 300 mg of liarozole was given on days 2 and 29, 1 hour before *at*RA. The simulation successfully predicted the DDI between *at*RA and liarozole in adult cancer patients with the exception of 150-mg liarozole dosing where the observed studies reported *at*RA AUCs that had acceptance ranges that excluded all other clinical observations (Table 6 and Fig. 5). The other predicted AUCs of *at*RA on each reported study day in the presence or absence of liarozole were within the predefined model acceptance criteria.

The simulation predicted about 61% decrease in *at*RA AUC between day 1 and day 28, a prediction in good agreement with the observed 58%–84% decrease in *at*RA AUC. The simulation

TABLE 6

Observed and predicted AUC of *at*RA in adult cancer patients in the presence of ketoconazole and liarozole (mean ± S.D.)

The ketoconazole study data are from Rigas et al. (1993), and liarozole data are from Miller et al. (1994). In the studies *at*RA was dosed for 29 days and ketoconazole or liarozole administered on days 2 and 29 while the control session pharmacokinetics studies were done on days 1 and 28.

Study	Study Day	*n*	AUC [*ng·h/ml*]		
			Observed	Predicted	Acceptance Range
Ketoconazole					
Dosing control	1	31	467 ± 469	517 ± 171	234–887
All dose levels combined	2	31	531 ± 522	724 ± 443	267–1009
200 mg study control	28	7	176 ± 141	201 ± 130	88–334
200 mg	29	7	262 ± 200	404 ± 239	131–498
400 mg study control	28	6	185 ± 190	205 ± 139	93–352
400 mg	29	6	400 ± 211	547 ± 296	200–760
Liarozole					
Dosing control	19	19	504 ± 549	533 ± 138	252–958
All dose levels combined	2	19	363 ± 358	482 ± 323	182–726
75 mg study control	28	5	210 ± 159	208 ± 134	105–399
75 mg	29	5	347 ± 329	257 ± 163	174–659
150 mg study control	28	8	78 ± 65	208 ± 131[a]	39–156
150 mg	29	8	135 ± 195	278 ± 169[a]	68–270
300 mg study control	28	6	140 ± 108	203 ± 130	70–280
300 mg	29	6	309 ± 138	307 ± 184	155–618

[a]Outside of the acceptance range.

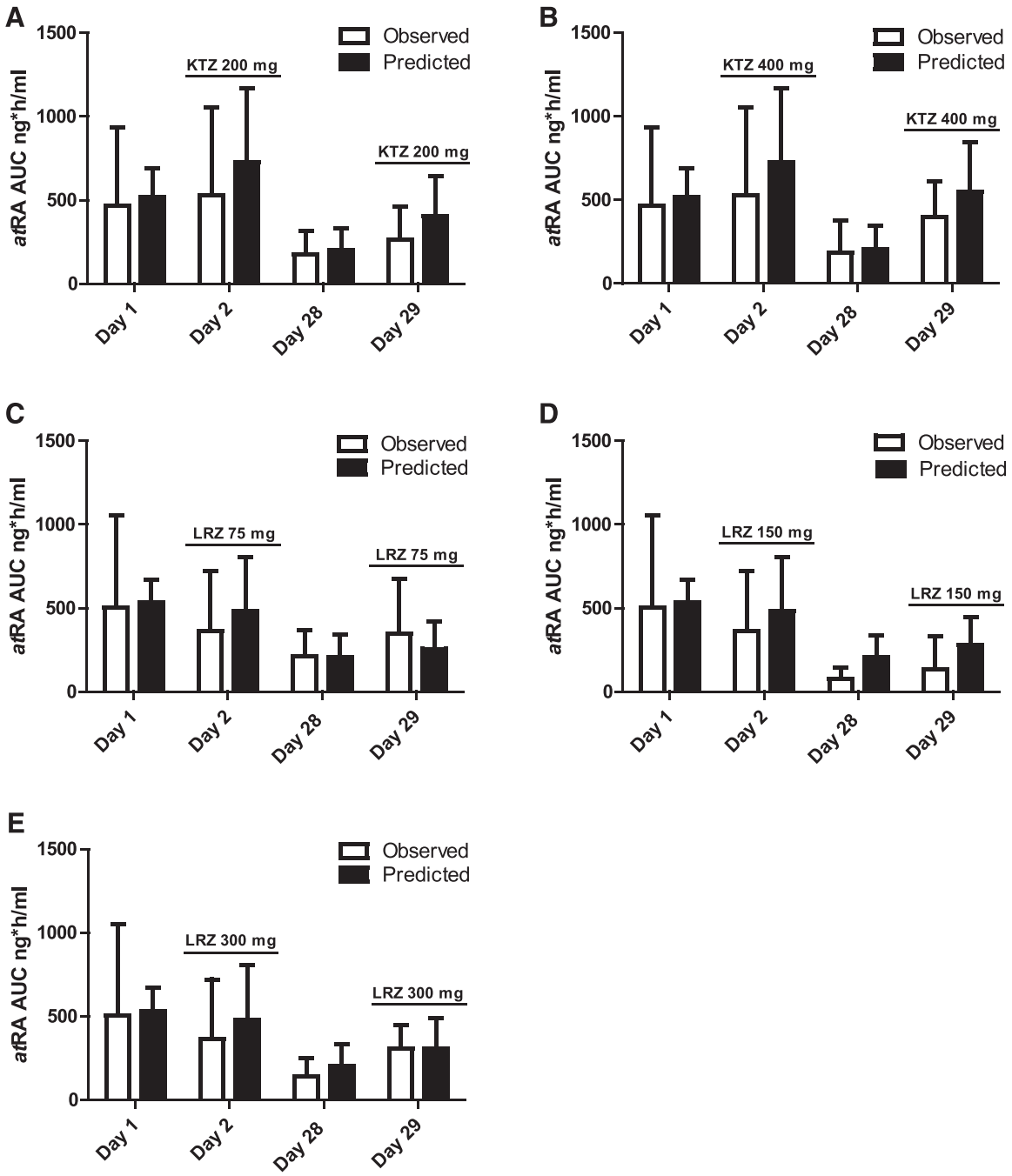

Fig. 5. Predicted (black bars) and observed (white bars) *at*RA AUC in cancer patients dosed with a single dose of 45 mg/m^2 of *at*RA on days 1, 2, 28, and 29, and twice a day for the rest of the days. A single dose of ketoconazole or liarozole was given on days 2 and 29 1 hour before *at*RA. Ketoconazole was dosed at (A) 200 mg and (B) 400 mg, and liarozole at (C) 75 mg, (D) 150 mg, and (E) 300 mg. The observed data are from Miller et al. (1994) and Rigas et al. (1993).

also correctly predicted that on day 2 despite the liarozole administration, the AUC of *at*RA would be lower or not different when compared with that on day 1 of treatment. Similarly, the simulation predicted a 1.2-fold to 1.5-fold increase in *at*RA AUC by liarozole dosing between day 28 and day 29, which is in excellent agreement with the 1.7-fold to 2.2-fold observed increase in *at*RA AUC (Table 6). The simulation also accurately predicted the efficacy of liarozole in combatting therapy resistance to *at*RA. The simulated data predicted that 300-mg liarozole would restore *at*RA AUC to 58% of the initial AUC after a single dose. This is in excellent agreement with the observed efficacy of liarozole restoring *at*RA AUC to 61% of that observed after single dose (Table 6).

Discussion

All-*trans* retinoic acid is widely used as a therapeutic agent in the treatment of APL and has shown promise in the treatment of other malignancies. However, the therapeutic use of *at*RA is limited due to its dose- and time-dependent kinetics. Although the dose- and time-dependent kinetics of *at*RA have been observed in animals and humans, the

mechanisms and kinetics of saturation and induction of *at*RA metabolism have not been well characterized in vivo. The PBPK model of *at*RA disposition presented here provides a mechanistic framework for understanding the time- and dose-dependent kinetics of therapeutically administered *at*RA.

Complex *at*RA kinetics were incorporated in the PBPK model and successfully simulated clinical studies after single and multiple doses of *at*RA both in healthy volunteers and in cancer patients. The simulations strongly support the hypothesis that the dose-dependent, nonlinear kinetics of *at*RA are due to saturation of CYP26A1-mediated clearance of *at*RA, and that the time dependent increase in *at*RA clearance is due to induction of hepatic CYP26A1 by *at*RA. It is possible that CYP26A1 is induced in other metabolic sites as well, but at present CYP26A1 expression appears to be restricted predominantly to the liver (Topletz et al., 2012). Taken together, the developed *at*RA PBPK model demonstrates a unique application of PBPK modeling to a complex clinical scenario of drug disposition including time- and concentration-dependent changes in clearance. The presented data show that in vitro data can successfully be used to develop PBPK models of such complex systems and incorporate new eliminating enzymes into existing models when adequate physiologic data are available.

At present, there is no appropriate dosage form of *at*RA to allow i.v. administration to humans, so the absorption and distribution kinetics of *at*RA are poorly understood. The studies presented here show that despite its high lipophilicity, *at*RA has relatively low permeability and a restricted volume of distribution similar to many other lipophilic acidic compounds that are highly bound to plasma albumin. The Caco-2 cell assay suggested that passive diffusion is the primary mechanism of *at*RA absorption in the gut and that transporters do not contribute to *at*RA absorption. The distribution volume of *at*RA appears to be predictable between species, and it is likely that the individual organ tissue to plasma partition ratios are similar between species. However, at present the distribution component of the PBPK model is not adequate to allow simulation of *at*RA distribution to specific organs or drug target sites except the liver, kidney, lung, pancreas, and brain.

The in vivo clearance of *at*RA was predicted from in vitro enzyme kinetic data with the addition of the in vivo information of lack of renal elimination of unchanged *at*RA and detection of conjugated metabolites such as glucuronides in human urine. The enzyme kinetic data and the dynamic model predicted approximately 90% clearance of *at*RA by hepatic CYP26A1 metabolism after a single dose of *at*RA, a value in good agreement with the previously predicted >90% contribution based on static prediction (Thatcher et al., 2010). Uniquely, this model also accurately predicted the saturation kinetics of *at*RA based on the in vitro enzyme kinetic values and the time-dependent induction of CYP26A1 based on HepG2 cell and hepatocyte induction data. In addition to *at*RA disposition when administered alone, the model also accurately predicted the complex DDIs between *at*RA and ketoconazole and *at*RA and liarozole.

The inhibition of *at*RA clearance has been an attractive therapeutic target for combating therapy resistance to *at*RA in treatment of APL and possibly other cancers. However, the development of inhibitors of *at*RA metabolism has been hindered by lack of understanding of the necessary potency and pharmacokinetic characteristics of novel inhibitors, especially in the target cancer population. The developed model together with the DDI simulations provides insight to the shortcomings of the clinical studies conducted with ketoconazole and liarozole as CYP26 inhibitors, and it will allow design of future dosing regimens that can restore *at*RA exposures to the levels observed after single doses. In addition, the model can be used to design *at*RA dosing regimens that achieve maximum exposure and efficacy.

It is well recognized that patient demographics and physiologic features are different for cancer patients and healthy subjects. To address these differences, a previously developed adult cancer population model (Cheeti et al., 2013) was adapted to test whether the healthy population PBPK model for *at*RA could be applied to cancer patients. Based on model verification and sensitivity analysis, all the data collectively suggested that *at*RA absorption is significantly decreased in cancer patients, while all the physiologic features reported in the previous cancer population model were applicable to the cancer populations included in the *at*RA clinical studies. The decrease in *at*RA absorption is not entirely surprising, as malnutrition, anorexia, and cachexia and alterations in nutrient absorption and nutritional status are commonly reported in cancer patients (Argilés, 2005). As *at*RA is also the active form of vitamin A, it is possible that alterations in its absorption are related to the general poor absorption of nutrients in cancer patients and will not reflect absorption processes for cancer medications. However, further studies are needed to investigate potential effects of cancer on drug absorption.

With the modification of the absorption of *at*RA in cancer patients, the developed PBPK model accurately predicted *at*RA disposition in this challenging patient population for which it is often difficult to obtain sufficient pharmacokinetic data. In addition, the developed PBPK model could be applied to predict *at*RA disposition in pediatric cancer patients, a uniquely vulnerable population. As such, the data obtained support the use of PBPK models developed in healthy populations to predict disposition in patient populations including pediatrics.

In summary, we have developed a mechanistic PBPK model predicting *at*RA disposition in both healthy volunteers and cancer patients. The model was successfully applied to simulate the pharmacokinetic profiles of *at*RA after single and multiple doses and to quantitatively predict the interaction between *at*RA and *at*RA metabolism inhibitors (ketoconazole and liarozole). Therefore, it could be used to investigate *at*RA disposition, to design drug-drug interaction studies in the development of novel *at*RA metabolism inhibitors, and to predict *at*RA pharmacokinetics in cancer patients.

Acknowledgments

The authors thank Michael D. Haenisch from the Department of Comparative Medicine at University of Washington for his skillful assistance in the mouse experiments.

Authorship Contributions

Participated in research design: Jing, Nelson, Shirasaka, Paik, Amory, Isoherranen.

Conducted experiments: Jing, Nelson, Amory, Paik, Shirasaka.

Performed data analysis: Jing, Nelson, Shirasaka, Isoherranen.

Wrote or contributed to the writing of the manuscript: Jing, Nelson, Shirasaka, Isoherranen.

References

Abduljalil K, Cain T, Humphries H, and Rostami-Hodjegan A (2014) Deciding on success criteria for predictability of pharmacokinetic parameters from in vitro studies: an analysis based on in vivo observations. *Drug Metab Dispos* **42**:1478–1484.

Ablain J and de The H (2011) Revisiting the differentiation paradigm in acute promyelocytic leukemia. *Blood* **117**:5795–5802.

Adamson PC (1996) All-trans-retinoic acid pharmacology and its impact on the treatment of acute promyelocytic leukemia. *Oncologist* **1**:305–314.

Adamson PC, Bailey J, Pluda J, Poplack DG, Bauza S, Murphy RF, Yarchoan R, and Balis FM (1995) Pharmacokinetics of all-trans-retinoic acid administered on an intermittent schedule. *J Clin Oncol* **13**:1238–1241.

Argilés JM (2005) Cancer-associated malnutrition. *Eur J Oncol Nurs* **9** (Suppl 2): S39–S50.

Arnold SLM, Amory JK, Walsh TJ, and Isoherranen N (2012) A sensitive and specific method for measurement of multiple retinoids in human serum with UHPLC-MS/MS. *J Lipid Res* **53**:587–598.

Arnold SLM, Kent T, Hogarth CA, Griswold MD, Amory JK, and Isoherranen N (2015) Pharmacological inhibition of ALDH1A in mice decreases all-trans retinoic acid concentrations in a tissue specific manner. *Biochem Pharmacol* **95**:177–192.

Arrieta O, González-De la Rosa CH, Aréchaga-Ocampo E, Villanueva-Rodríguez G, Cerón-Lizárraga TL, Martínez-Barrera L, Vázquez-Manríquez ME, Ríos-Trejo MA, Alvarez-Avitia MA, Hernández-Pedro N, et al. (2010) Randomized phase II trial of all-trans-retinoic acid with chemotherapy based on paclitaxel and cisplatin as first-line treatment in patients with advanced non-small-cell lung cancer. *J Clin Oncol* **28**:3463–3471.

Baxter JG, Brass C, Schentag JJ, and Slaughter RL (1986) Pharmacokinetics of ketoconazole administered intravenously to dogs and orally as tablet and solution to humans and dogs. *J Pharm Sci* **75**:443–447.

Bryson HM and Wagstaff AJ (1996) Liarozole. *Drugs Aging* **9**:478–484.

Cheeti S, Budha NR, Rajan S, Dresser MJ, and Jin JY (2013) A physiologically based pharmacokinetic (PBPK) approach to evaluate pharmacokinetics in patients with cancer. *Biopharm Drug Dispos* **34**:141–154.

Clewell, 3rdHJ, Andersen ME, Wills RJ, and Latriano L (1997) A physiologically based pharmacokinetic model for retinoic acid and its metabolites. *J Am Acad Dermatol* **36**:S77–S85.

Conley BA, Egorin MJ, Sridhara R, Finley R, Hemady R, Wu S, Tait NS, and Van Echo DA (1997) Phase I clinical trial of all-trans-retinoic acid with correlation of its pharmacokinetics and pharmacodynamics. *Cancer Chemother Pharmacol* **39**:291–299.

Coombs CC, Tavakkoli M, and Tallman MS (2015) Acute promyelocytic leukemia: where did we start, where are we now, and the future. *Blood Cancer J* **5**:e304.

Daneshmend TK, Warnock DW, Ene MD, Johnson EM, Potten MR, Richardson MD, and Williamson PJ (1984) Influence of food on the pharmacokinetics of ketoconazole. *Antimicrob Agents Chemother* **25**:1–3.

Daneshmend TK, Warnock DWTA, Turner A, and Roberts CJ (1981) Pharmacokinetics of ketoconazole in normal subjects. *J Antimicrob Chemother* **8**:299–304.

De Buck SS, Sinha VK, Fenu LA, Gilissen RA, Mackie CE, and Nijsen MJ (2007) The prediction of drug metabolism, tissue distribution, and bioavailability of 50 structurally diverse compounds in rat using mechanism-based absorption, distribution, and metabolism prediction tools. *Drug Metab Dispos* **35**:649–659.

Denis L, Debruyne F, De Porre P, and Bruynseels J (1998) Early clinical experience with liarozole (Liazal) in patients with progressive prostate cancer. *Eur J Cancer* **34**:469–475.

Huang YC, Colaizzi JL, Bierman RH, Woestenborghs R, and Heykants J (1986) Pharmacokinetics and dose proportionality of ketoconazole in normal volunteers. *Antimicrob Agents Chemother* **30**:206–210.

Jing J, Isoherranen N, Robinson-Cohen C, Petrie I, Kestenbaum BR, and Yeung CK (2016) Chronic kidney disease alters vitamin A homeostasis via effects on hepatic RBP4 protein expression and metabolic enzymes. *Clin Transl Sci* **9**:207–215.

Jones HM, Chen Y, Gibson C, Heimbach T, Parrott N, Peters SA, Snoeys J, Upreti VV, Zheng M, and Hall SD (2015) Physiologically based pharmacokinetic modeling in drug discovery and development: a pharmaceutical industry perspective. *Clin Pharmacol Ther* **97**:247–262.

Lee JS, Newman RA, Lippman SM, Fossella FV, Calayag M, Raber MN, Krakoff IH, and Hong WK (1995) Phase I evaluation of all-trans retinoic acid with and without ketoconazole in adults with solid tumors. *J Clin Oncol* **13**:1501–1508.

Lim YC, Kang HJ, Kim YS, and Choi EC (2012) All-trans-retinoic acid inhibits growth of head and neck cancer stem cells by suppression of Wnt/β-catenin pathway. *Eur J Cancer* **48**:3310–3318.

Louisse J, Bosgra S, Blaauboer BJ, Rietjens IMCM, and Verwei M (2015) Prediction of in vivo developmental toxicity of all-trans-retinoic acid based on in vitro toxicity data and in silico physiologically based kinetic modeling. *Arch Toxicol* **89**:1135–1148.

Lutz JD, Dixit V, Yeung CK, Dickmann LJ, Zelter A, Thatcher JE, Nelson WL, and Isoherranen N (2009) Expression and functional characterization of cytochrome P450 26A1, a retinoic acid hydroxylase. *Biochem Pharmacol* **77**:258–268.

Lutz JD and Isoherranen N (2012) In vitro-to-in vivo predictions of drug-drug interactions involving multiple reversible inhibitors. *Expert Opin Drug Metab Toxicol* **8**:449–466.

Miller VA, Rigas JR, Muindi JRF, Tong WP, Venkatraman E, Kris MG, and Warrell, JrRP (1994) Modulation of all-trans retinoic acid pharmacokinetics by liarozole. *Cancer Chemother Pharmacol* **34**:522–526.

Muindi J, Frankel SR, Miller, JrWH, Jakubowski A, Scheinberg DA, Young CW, Dmitrovsky E, and Warrell, JrRP (1992a) Continuous treatment with all-trans retinoic acid causes a progressive reduction in plasma drug concentrations: implications for relapse and retinoid "resistance" in patients with acute promyelocytic leukemia. *Blood* **79**:299–303.

Muindi JR, Frankel SR, Huselton C, DeGrazia F, Garland WA, Young CW, and Warrell, JrRP (1992b) Clinical pharmacology of oral all-trans retinoic acid in patients with acute promyelocytic leukemia. *Cancer Res* **52**:2138–2142.

Muindi JR, Young CW, and Warrell, JrRPJ (1994) Clinical pharmacology of all-trans retinoic acid. *Leukemia* **8**:1807–1812.

Nakai D, Kumamoto K, Sakikawa C, Kosaka T, and Tokui T (2004) Evaluation of the protein binding ratio of drugs by a micro-scale ultracentrifugation method. *J Pharm Sci* **93**:847–854.

Nelson CH, Buttrick BR, and Isoherranen N (2013) Therapeutic potential of the inhibition of the retinoic acid hydroxylases CYP26A1 and CYP26B1 by xenobiotics. *Curr Top Med Chem* **13**:1402–1428.

Njar VC, Gediya L, Purushottamachar P, Chopra P, Vasaitis TS, Khandelwal A, Mehta J, Huynh C, Belosay A, and Patel J (2006) Retinoic acid metabolism blocking agents (RAMBAs) for treatment of cancer and dermatological diseases. *Bioorg Med Chem* **14**:4323–4340.

Ozpolat B, Lopez-Berestein G, Adamson P, Fu CJ, and Williams AH (2003) Pharmacokinetics of intravenously administered liposomal all-trans-retinoic acid (ATRA) and orally administered ATRA in healthy volunteers. *J Pharm Pharm Sci* **6**:292–301.

Peng J-B, Luo C-H, Wang Y-C, Huang W-H, Chen Y, Zhou H-H, and Tan Z-R (2014) Validation of a liquid chromatography-electrospray ionization-tandem mass spectrometry method for determination of all-trans retinoic acid in human plasma and its application to a bioequivalence study. *Molecules* **19**:1189–1200.

Phuphanich S, Scott C, Fischbach AJ, Langer C, and Yung WK (1997) All-trans-retinoic acid: a phase II Radiation Therapy Oncology Group study (RTOG 91-13) in patients with recurrent malignant astrocytoma. *J Neurooncol* **34**:193–200.

Regazzi MB, Iacona I, Gervasutti C, Lazzarino M, and Toma S (1997) Clinical pharmacokinetics of tretinoin. *Clin Pharmacokinet* **32**:382–402.

Rigas JR, Miller VA, Zhang ZF, Klimstra DS, Tong WP, Kris MG, and Warrell, JrRP (1996) Metabolic phenotypes of retinoic acid and the risk of lung cancer. *Cancer Res* **56**:2692–2696.

Rigas JR, Francis PA, Muindi JR, Kris MG, Huselton C, DeGrazia F, Orazem JP, Young CWWRJ, and Warrell, JrRP (1993) Constitutive variability in the pharmacokinetics of the natural retinoid, all-trans-retinoic acid, and its modulation by ketoconazole. *J Natl Cancer Inst* **85**:1921–1926.

Rodgers T and Rowland M (2006) Physiologically based pharmacokinetic modelling 2: predicting the tissue distribution of acids, very weak bases, neutrals and zwitterions. *J Pharm Sci* **95**:1238–1257.

Russo D, Regazzi M, Sacchi S, Visani G, Lazzarino M, Avvisati G, Pelicci PG, Dastoli G, Grandi C, Iacona I, et al. (1998) All-trans retinoic acid (ATRA) in patients with chronic myeloid leukemia in the chronic phase. *Leukemia* **12**:449–454.

Saadeddin A,Torres-Molina F, Cárcel-Trullols J, Araico A, and Peris JE (2004) Pharmacokinetics of the time-dependent elimination of all-trans-retinoic acid in rats. *AAPS PharmSci* **6**:E1.

Saiag P, Pavlovic M, Clerici T, Feauveau V, Nicolas JC, Emile D, and Chastang C (1998) Treatment of early AIDS-related Kaposi's sarcoma with oral all-trans-retinoic acid: results of a sequential non-randomized phase II trial. Kaposi's Sarcoma ANRS Study Group. Agence Nationale de Recherches sur le SIDA. *AIDS* **12**: 2169–2176.

Sandberg JA, Eckhoff C, Nau H, and Slikker, JrW (1994) Pharmacokinetics of 13-cis-, all-trans-, 13-cis-4-oxo-, and all-trans-4-oxo retinoic acid after intravenous administration in the cynomolgus monkey. *Drug Metab Dispos* **22**: 154–160.

Shirasaka Y, Sager JE, Lutz JD, Davis C, and Isoherranen N (2013) Inhibition of CYP2C19 and CYP3A4 by omeprazole metabolites and their contribution to drug-drug interactions. *Drug Metab Dispos* **41**:1414–1424.

Smith MA, Adamson PC, Balis FM, Feusner J, Aronson L, Murphy RF, Horowitz ME, Reaman G, Hammond GD, and Fenton RM (1992) Phase I and pharmacokinetic evaluation of all-trans-retinoic acid in pediatric patients with cancer. *J Clin Oncol* **10**:1666–73.

Takitani K, Tamai H, Morinobu T, Kawamura N, Miyake M, Fujimoto T, and Mino M (1995) Pharmacokinetics of All- trans Retinoic Acid in Pediatric Patients with Leukemia. Japanese *J Cancer Res* **86**:400–405.

Tay S, Dickmann L, Dixit V, and Isoherranen N (2010) A comparison of the roles of peroxisome proliferator-activated receptor and retinoic acid receptor on CYP26 regulation. *Mol Pharmacol* **77**:218–227.

Thatcher JE, Buttrick B, Shaffer SA, Shimshoni JA, Goodlett DR, Nelson WL, and Isoherranen N (2011) Substrate specificity and ligand interactions of CYP26A1, the human liver retinoic acid hydroxylase. *Mol Pharmacol* **80**:228–239.

Thatcher JE, Zelter A, and Isoherranen N (2010) The relative importance of CYP26A1 in hepatic clearance of all-trans retinoic acid. *Biochem Pharmacol* **80**: 903–912.

Thudi NR, Shrivastav VK, Monif T, Khuroo A, Gurule S, Partani PO, Tandon M, and Mathur R (2011) Pharmacokinetic and bioequivalence study of endogenous compound tretinoin 10 mg capsules in healthy volunteers by base line correction approach. *Clin Res Regul Aff* **28**:68–73 DOI: 10.3109/10601333.2011.597762.

Topletz AR, Thatcher JE, Zelter A, Lutz JD, Tay S, Nelson WL, and Isoherranen N (2012) Comparison of the function and expression of CYP26A1 and CYP26B1, the two retinoic acid hydroxylases. *Biochem Pharmacol* **83**:149–163.

Topletz AR, Tripathy S, Foti RS, Shimshoni JA, Nelson WL, and Isoherranen N (2015) Induction of CYP26A1 by metabolites of retinoic acid: evidence that CYP26A1 is an important enzyme in the elimination of active retinoids. *Mol Pharmacol* **87**:430–441.

Wang CC, Campbell S, Furner RL, and Hill DL (1980) Disposition of all-trans- and 13-cis-retinoic acids and n-hydroxyethylretinamide in mice after intravenous administration. *Drug Metab Dispos* **8**:8–11.

Address correspondence to: Dr. Nina Isoherranen, University of Washington Health Science Building Room H-272M Box 357610, Seattle, WA 98195-7610. E-mail: ni2@uw.edu